

Modeling the superstorm in November 2003

Mei-Ching Fok,¹ Thomas E. Moore,¹ Steve P. Slinker,² Joel A. Fedder,³
Dominique C. Delcourt,⁴ Masahito Nosé,⁵ and Sheng-Hsien Chen¹

Received 26 May 2010; revised 30 September 2010; accepted 6 October 2010; published 7 January 2011.

[1] The superstorm on 20–21 November 2003 was the largest geomagnetic storm in solar cycle 23 as measured by Dst, which attained a minimum value of -422 nT. We have simulated this storm to understand how particles originating from the solar wind and ionosphere get access to the magnetosphere and how the subsequent transport and energization processes contribute to the buildup of the ring current. The global electromagnetic configuration and the solar wind H^+ distribution are specified by the Lyon-Fedder-Mobarry (LFM) magnetohydrodynamics model. The outflow of H^+ and O^+ ions from the ionosphere are also considered. Their trajectories in the magnetosphere are followed by a test-particle code. The particle distributions at the inner plasma sheet established by the LFM model and test-particle calculations are then used as boundary conditions for a ring current model. Our simulations reproduce the rapid decrease of Dst during the storm main phase and the fast initial phase of recovery. Shielding in the inner magnetosphere is established at early main phase. This shielding field lasts several hours and then breaks down at late main phase. At the peak of the storm, strong penetration of ions earthward to L shell of 1.5 is revealed in the simulation. It is surprising that O^+ is significant but not the dominant species in the ring current in our calculation for this major storm. It is very likely that substorm effects are not well represented in the models and O^+ energization is underestimated. Ring current simulation with O^+ energy density at the boundary set comparable to Geotail observations produces excellent agreement with the observed symH. As expected in superstorms, ring current O^+ is the dominant species over H^+ during the main to midrecovery phase of the storm.

Citation: Fok, M.-C., T. E. Moore, S. P. Slinker, J. A. Fedder, D. C. Delcourt, M. Nosé, and S.-H. Chen (2011), Modeling the superstorm in November 2003, *J. Geophys. Res.*, 116, A00J17, doi:10.1029/2010JA015720.

1. Introduction

[2] The magnetic storm on 20–21 November 2003 is the greatest storm in solar cycle 23 as measured by the Dst index. At 2100 UT on 20 November, Dst attained a minimum value of -422 nT. This superstorm was triggered by a fast coronal mass ejection carrying high-speed solar wind and strong southward interplanetary magnetic field (IMF) near the Earth. Figure 1 shows the Dst index on 20–21 November 2003 together with solar wind speed, density, B_z and B_y at L1 from the ACE satellite. The ACE data have been shifted by 40 min. Pronounced storm signatures were observed in both the magnetosphere and ionosphere-thermosphere during this superstorm. Bortnik *et al.* [2006] found large relativistic electron dropout on 20 November

2003 from a number of satellites. They suggested that dropout at $L > 5$ was mainly from losses at the dayside magnetopause. The flux decrease at $L < 5$ was energy dependent with larger loss for higher-energy electrons. Strong precipitation was seen on the duskside near the plasmapause and plume. Bortnik *et al.* [2006] concluded that pitch angle scattering from interactions with electromagnetic ion cyclotron (EMIC) waves were responsible for electrons losses at low L shells. The disappearance of proton belt at $L > 2.2$ was also observed from the HEO3 satellite (R. Selesnick, private communication, 2009). Identifying the cause of the proton detrapping during this great event is still underway. Thermospheric composition changes were seen on 20 November 2003 [Hecht *et al.*, 2008]. Large depletion of atomic oxygen was correlated with Joule heating and auroral particle precipitation. Foster *et al.* [2005] examined the 2-D maps of vertical total electron content (TEC) derived from a network of GPS receivers. Near the peak of the storm, they saw continuous plume of enhanced TEC extended to high latitudes in the postnoon sector. This polar tongue of ionization is believed carried by strong convection through the dayside cusp and across the polar cap to the nightside. Meanwhile, prompt penetration electric (PPE) fields at midlatitudes to low latitudes were reported by Zhao *et al.* [2008]. They found PPE occurred when IMF

¹NASA Goddard Space Flight Center, Greenbelt, Maryland, USA.

²Naval Research Laboratory, Washington, D. C., USA.

³Leading Edge Technology, Inc., Alexandria, Virginia, USA.

⁴Laboratoire de Physique des Plasmas, UMR 7648, Ecole Polytechnique, CNRS, Saint-Maur-des-Fossés, France.

⁵Data Analysis Center for Geomagnetism and Space Magnetism, Graduate School of Science, Kyoto University, Kyoto, Japan.

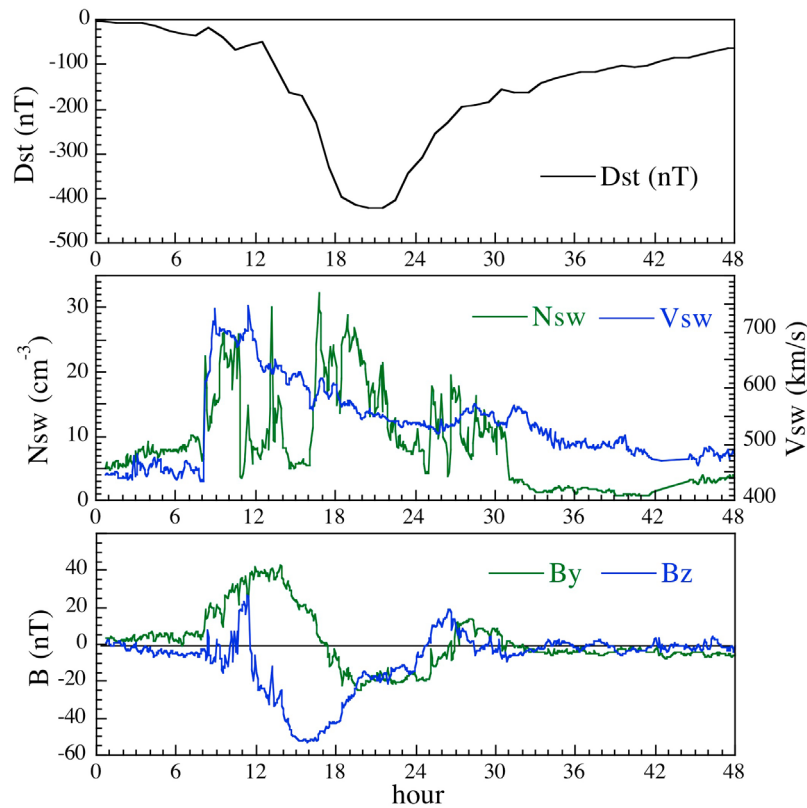


Figure 1. (top) Dst and (middle and bottom) solar wind parameters from the ACE satellite on 20–21 November 2003. Zero hour corresponds to 0000 UT on 20 November. The ACE data have been shifted by 40 min.

turned strongly southward at ~ 1200 UT on 20 November and it lasted for about 12 h. We have previously modeled this great magnetic storm on 20–21 November 2003 [Ebihara *et al.*, 2005]. The Comprehensive Ring Current Model (CRCM) [Fok *et al.*, 2001] and magnetic field model of Tsyganenko 1996 (T96) [Tsyganenko and Stern, 1996] were used to simulate the responses of the ring current and the magnetosphere-ionosphere system to severe disturbances associated with passing of a magnetic cloud. Only ring current H^+ was considered in the calculation. A number of distinct storm signatures were successfully identified and reproduced. We found deep earthward penetration of ring current ions to $L \leq 1.5$ and a robust ring current that could account for the observed Dst. Both simulation and observation showed equatorward extension of Region 2 current down to 40° magnetic latitude. The shielding field generated by this strong field aligned current distorted the convection and flow patterns in the ionosphere. A noticeable feature was the flow reversal on the dawnside ionosphere. In this paper, we revisit this distinct storm event in November 2003 using our Global Ion Kinetic (GIK) simulation [Moore *et al.*, 2008]. We simulate the global magnetospheric configuration using the Lyon-Fedder-Mobarry (LFM) magnetohydrodynamic (MHD) model [Fedder *et al.*, 1995; Mobarry *et al.*, 1996; Slinker *et al.*, 2001]. The LFM density and temperature in the magnetosphere represent ions of solar wind source. In addition to H^+ from the solar wind, O^+ and H^+ outflow from the ionosphere are also considered. We follow the full-particle trajectories of the ionospheric ions from their source

regions throughout the magnetosphere. Some of the ions are lost in the solar wind, however, a significant portion are trapped in the plasma sheet and has access to the inner magnetosphere. As in our previous study [Fok *et al.*, 2006; Moore *et al.*, 2008], the CRCM is used to simulate the ring current development and evolutions of the Region 2 current and subauroral convection field. The ion distributions at the CRCM outer boundary at 8 earth radii (R_E) are given by the LFM model (solar wind H^+) and by the density and temperature established from the test-particle calculations (ionospheric H^+ and O^+). We examine the relative roles of ions from various sources in the intensification of the ring current, especially the contribution of oxygen ions. We identify the processes that are responsible for the storm recovery. We also follow the establishment and breakdown of the shielding field in the inner magnetosphere. In the following sections, we will briefly describe our simulation tools and approaches. We then highlight the signatures seen in the simulation and confront the findings with available data.

2. Global Magnetospheric Simulation on 20–21 November 2003

2.1. LFM Simulation

[3] We simulate the global magnetospheric configuration during the storm on 20–21 November 2003 using the LFM model [Fedder *et al.*, 1995; Mobarry *et al.*, 1996; Slinker *et al.*, 1998]. The LFM model takes the upstream solar wind conditions and solves the ideal MHD equations in a distorted

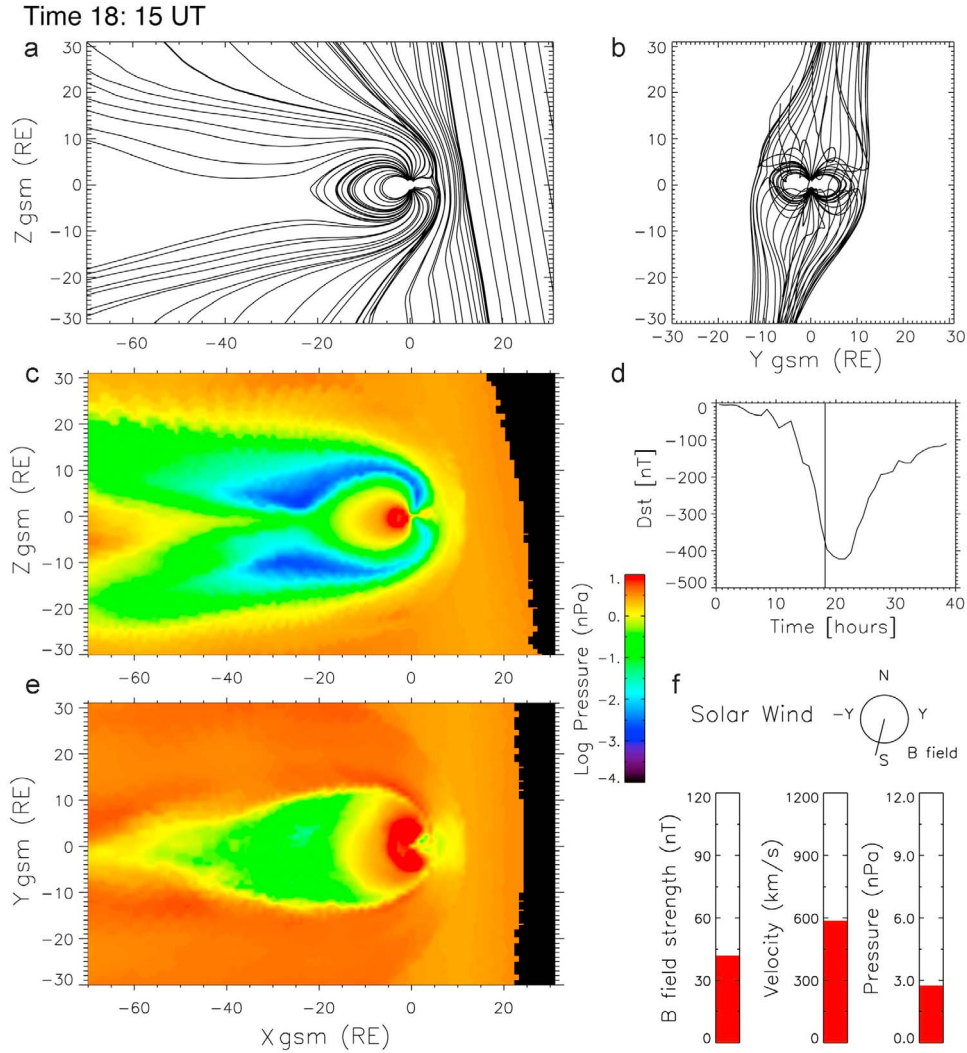


Figure 2. Global magnetospheric configuration at 1815 UT on 20 November 2003 predicted by the LFM Model. (a and b) Magnetic field lines. (c and e) LFM pressure. (d and f) Dst index and solar wind condition.

spherical grid that extends $24 R_E$ sunward of the Earth to $300 R_E$ tailward and $90 R_E$ in the Y and Z direction. The inner boundary is a sphere with a radius of $3.2 R_E$ centered on the Earth. Field-aligned currents are mapped from this boundary to the ionosphere, where electric potential is solved. The solution for the potential then provides an electric field that is mapped back to the inner boundary where it is used as a boundary condition for the MHD evolution. The LFM output (temperature, density and pressure) in the magnetosphere are used for particle distribution of H^+ ions of solar wind source.

[4] Figure 2 shows the global magnetospheric configuration near the peak of the storm at 1815 UT on 20 November 2003 as predicted by the LFM model. The Dst index and solar wind condition are plotted in Figures 2d and 2f. Figures 2a and 2b depict the solar wind magnetic field lines and geomagnetic field lines that have at least one ionospheric foot point. At this time, IMF was strongly southward with a magnitude of nearly 40 nT. The high solar wind pressure and strong reconnection on the dayside pretty much

open up the magnetosphere around the subsolar point (Figure 2a). Figures 2c and 2e are MHD pressure on the $X-Z$ and $X-Y$ planes, respectively. An X line is formed at $\sim 25 R_E$ on the nightside. Tailward to the X line there is a high-pressure region of down streaming plasma. In the meantime, high pressure has established in the inner magnetosphere.

2.2. Ion Outflow From the Ionosphere

[5] In addition to solar wind ions, we also consider ions from the ionospheric sources. We will examine their roles in the development of the storm in November 2003. Similar to our previous study [Moore *et al.*, 2008], we release H^+ and O^+ ions from the ionosphere and follow their trajectories throughout the magnetosphere using a test-particle code [Delcourt *et al.*, 1990] during the event until they are lost in the solar wind or at the surface of the Earth. The simulation domain for particle tracing is bounded by $X = -70$ and $15 R_E$, $Y = -30$ and $30 R_E$, and $Z = -30$ and $30 R_E$.

[6] We employ the same outflow condition for ionospheric H^+ and O^+ as in our previous studies [Moore *et al.*, 2007].

Ions are released at both hemispheres at 1000 km altitude at latitudes greater than 60°. The flux of the polar wind H^+ outflow depends on solar zenith angle (SZA) with much higher flux on the dayside than on the nightside [Su *et al.*, 1998; Moore *et al.*, 2007]:

$$\begin{aligned} F_{H^+} &= 2 \times 10^8 \text{ cm}^{-2} \text{ s}^{-1} & \text{for } 0^\circ < \text{SZA} < 90^\circ \\ F_{H^+} &= 2 \times 10^{(8-(\text{SZA}-90)/20 \times 2.5)} \text{ cm}^{-2} \text{ s}^{-1} & \text{for } 90^\circ \leq \text{SZA} \leq 110^\circ \\ F_{H^+} &= 2 \times 10^{5.5} \text{ cm}^{-2} \text{ s}^{-1} & \text{for } 110^\circ < \text{SZA} < 180^\circ \end{aligned} \quad (1)$$

The O^+ escape flux is found to be sensitive to the energy input from the magnetosphere and solar wind. By analyzing data from the FAST and POLAR missions, it was suggested that two major energy sources are the electron precipitation and dissipation of downward Poynting flux [Strangeway *et al.*, 2005; Zheng *et al.*, 2005]. We model the local O^+ outflow flux in the same way as Moore *et al.* [2007]:

$$F_{O^+} = (F_{\text{precip}} \times F_{\text{poynt}})^{0.5} \quad \text{subject to a limit of } 3 \times 10^9 \text{ cm}^{-2} \text{ s}^{-1} \quad (2)$$

where

$$\begin{aligned} F_{\text{precip}} &= 2.8 \times 10^9 \times N^{2.2} \text{ cm}^{-2} \text{ s}^{-1} \\ F_{\text{poynt}} &= 5.6 \times 10^7 \times (0.245 \times S_{120})^{1.26} \text{ cm}^{-2} \text{ s}^{-1} \\ N &= n \cdot \left(1 - \text{erf} \left(\sqrt{\frac{50}{T}} \right) \right) \cdot (0.4(1 + 0.8 \sin(2\pi(\text{MLT} - 3)/24))) \end{aligned}$$

N is the reduced MHD density (n) in cm^{-3} at the LFM inner boundary at 3.2 R_E . n is reduced to the fraction of density above 50 eV and by a loss cone filling factor. The first reduction comes from energy cutoff at 50 eV to remove photoelectron contamination of the FAST electron electrostatic analyzer [Strangeway *et al.*, 2005]. The second reduction considers the scattering rate by waves of magnetospheric electrons into the loss cone [Chen and Schulz, 2001]. S_{120} in equation (2) is the LFM Poynting flux in mWm^{-2} at 120 km altitude. The constant 0.245 is the scaling factor of energy flux mapping along a flux tube from 120 km to the FAST altitude (4000 km) [Strangeway *et al.*, 2000, 2005]. We combine the effects of electron precipitation and Poynting flux by taking geometric mean of F_{precip} and F_{poynt} . The local O^+ escape flux is limited to $3 \times 10^9 \text{ cm}^{-2} \text{ s}^{-1}$ based on the concept from ionospheric theory [Barakat *et al.*, 1987], and the highest fluxes observed by Strangeway *et al.* [2005].

[7] The thermal energy of the upwelling H^+ and O^+ is assumed to have a dependence on Poynting flux as [Moore *et al.*, 2007]

$$E_{th} = 0.1 + 9.23 \times (0.245 \times S_{120})^{0.35} \text{ eV} \quad (3)$$

The parallel energy is assigned as the sum of thermal energy and parallel energy given from the auroral parallel potential drop, which is scaled with the upward parallel current density as [Lyons, 1981]

$$E_{\parallel} = E_{th} + e\Phi_{\parallel} \quad (4)$$

where

$$\begin{aligned} \Phi_{\parallel} &= 1500 \times (J_{\parallel} - 0.33)^2 & \text{if } J_{\parallel} > 0.33 \text{ } \mu\text{A/m}^2 \\ \Phi_{\parallel} &= 0 & \text{if } J_{\parallel} < 0.33 \text{ } \mu\text{A/m}^2 \end{aligned}$$

Figure 3 (bottom) shows the simulated O^+ outflow conditions at 1000 km altitude at 1815 UT on 20 November 2003 during the main phase of the storm. Figure 3 (top) is LFM parameters that control the outflow flux and escape energy. Sun is up in the plots. It can be seen that at this particular time, O^+ ions attain high upward energy in the noon-dusk sector at 60°–80° latitudes (Figure 3, bottom right). Most of them escape from the ionosphere and travel through the lobes to the plasma sheet and the inner magnetosphere. During their journey they gain energy and become part of the ring current population [Fok *et al.*, 2006].

[8] We release ions from the ionosphere randomly in time, latitude and gyrophase angle. Similar to the approach of Fok *et al.* [2006] and Moore *et al.* [2008], the simulation domain is divided into volume elements of 1 R_E^3 and time in intervals of Δt . The density in volume bin j at time t contributed by particle i , which passes through bin j between $(t - 0.5 \Delta t)$ and $(t + 0.5 \Delta t)$, is given by

$$n_{ij}(t) = F_i(t_i) |\cos \alpha_i(t_i)| dA \frac{T_{ij}}{V_j}; \quad dA = \frac{A}{N_{\Delta t}} \quad (5)$$

where F_i is the ion source flux, which is a function of t_i , the time particle i is launched, α_i is the initial pitch angle, dA is the area of the source surface allocated to each particle, that is the total source surface area, A , divided by number of particles launched in Δt ($N_{\Delta t}$), T_{ij} is residence time of particle i in bin j , and V_j is the volume of bin j , that is 1 R_E^3 in our case. The density in bin j at time t is just the summation of all particles that pass through bin j between $(t - 0.5 \Delta t)$ and $(t + 0.5 \Delta t)$. The pressure at bin j is given by

$$\begin{aligned} P_j(t) &= P_{\perp j}(t) + P_{\parallel j}(t) = \frac{2}{3} \sum_i n_{ij}(t) E_{ij}(t) \sin^2 \alpha_{ij}(t) \\ &+ \frac{2}{3} \sum_i n_{ij}(t) E_{ij}(t) \cos^2 \alpha_{ij}(t) \end{aligned} \quad (6)$$

where E_{ij} and α_{ij} are the energy and pitch angle of particle i in bin j , respectively.

[9] Using the method outlined in equations (5) and (6), we calculate the density, energy and pressure of ionospheric H^+ and O^+ throughout the magnetosphere. Figure 4 plots the O^+ pressure on the $X-Z$, $X-Y$ and $Y-Z$ planes at the same time as those in Figures 2 and 3 near the peak of the storm. The pressure in the plasma sheet and the inner magnetosphere is comparable with the H^+ pressure shown in Figure 2. A distinct feature of X line is also found at $\sim 25 R_E$ in the tail (Figure 4a). The long stripe seen in the south parts of Figure 4a and Figure 4c are outflow ions encountering the magnetopause reconnection region and are pulled both tailward and dawnward. At this time of the year, the northern hemisphere is tilted toward the nightside and southern tilted toward the

Time 18: 15 UT

Nov03 North MHD Conditions

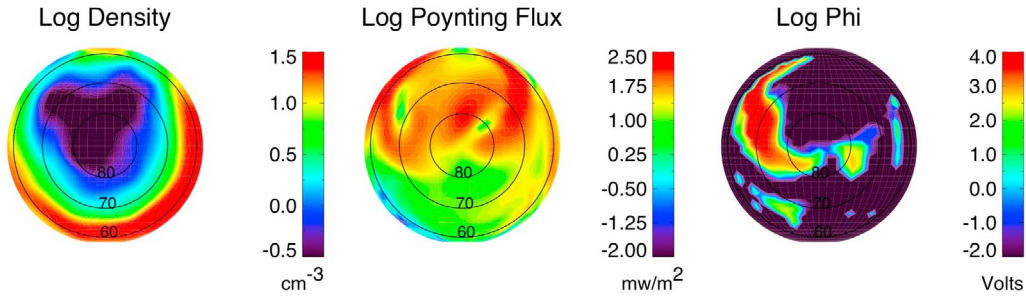
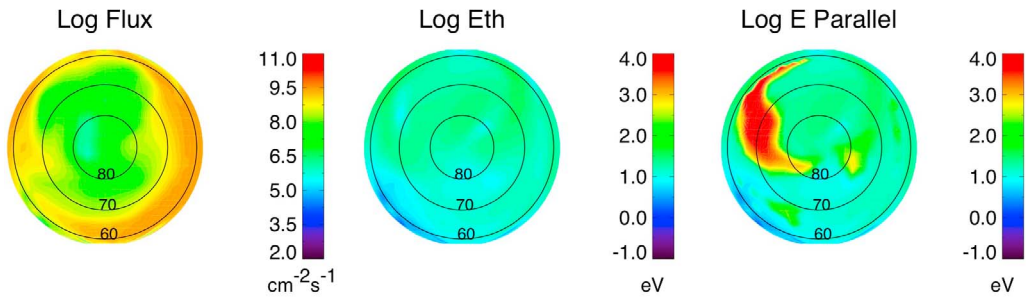
O⁺ Outflow Parameters

Figure 3. (top) MHD conditions at the ionosphere and (bottom) O⁺ outflow parameters at 1000 km altitude at 1815 UT on 20 November 2003. Sun is up in the plots.

Sun. Oxygen ions escaping from the southern ionosphere are easily picked up by the solar wind and are lost in the downstream. On the other hand, more ions outflow from the northern hemisphere manage to travel through the lobe and

reach to the plasmas sheet. As seen in Figure 4a, the O⁺ pressure in the northern lobe is higher than that in the south. The H⁺ outflow from the ionosphere in this particular storm contributes insignificantly to the H⁺ pressure (results not

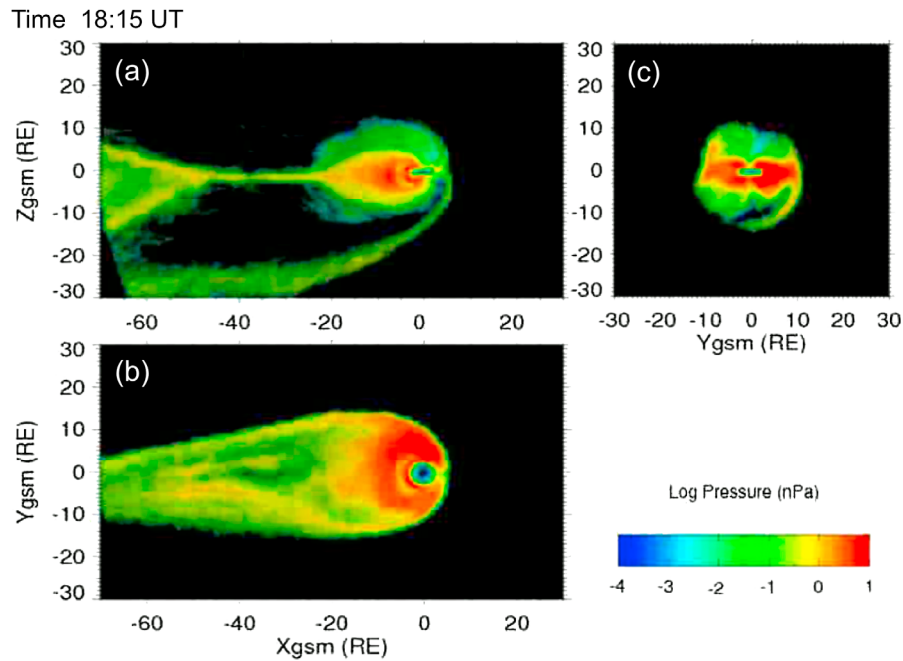


Figure 4. Calculated O⁺ pressure at 1815 UT on 20 November 2003.

shown) compared with ions of solar wind origin. A substantial fraction of this outflowing H^+ was found to enter the magnetosheath via high-latitude reconnection and to escape from the system downstream.

3. CRCM Simulation of the 20–21 November 2003 Storm

[10] Similar in our previous studies [Fok et al., 2006; Moore et al., 2008], we use the density and mean energy at the inner plasma sheet of ions of both solar wind and ionospheric origins as boundary conditions to the CRCM ring current model. Since the mean energies of ionospheric ions are calculated from the test-particle code (equation 6), we have considered the pitch angle information and assume the distribution at the CRCM boundary is a bi-Maxwellian [Fok et al., 2006]. The magnetic field in the inner magnetosphere is specified by the LFM model. The CRCM then calculates the ion distribution in the inner magnetosphere and the ionospheric potentials in a self-consistent manner. The two main equations solved by the CRCM are [Fok et al., 2001]

$$\frac{\partial f_s}{\partial t} + \langle \dot{\lambda}_i \rangle \frac{\partial f_s}{\partial \lambda_i} + \langle \dot{\phi}_i \rangle \frac{\partial f_s}{\partial \phi_i} = -v\sigma_{sH} \langle n_H \rangle f_s - \left(\frac{f_s}{0.5\tau_b} \right)_{\text{loss cone}} \quad (7)$$

$$\nabla \cdot \left(-\vec{\Sigma} \nabla \Phi \right) = J_{\parallel} \sin I \quad (8)$$

where f_s is the distribution function of ring current species s . λ_i and ϕ_i are the magnetic latitude and local time at the ionosphere, respectively. f_s is a function of λ_i , ϕ_i , first and second adiabatic invariants, and is assumed to be constant along a field line. Equatorial fluxes can be obtained by mapping f_s along field lines from the ionospheric grid to the equator. $\langle \dot{\lambda}_i \rangle$ and $\langle \dot{\phi}_i \rangle$ are the bounce-averaged velocities of species s on the ionospheric grid. σ_{sH} is charge exchange cross section for the ring current species s with neutral H. $\langle n_H \rangle$ is the bounce-averaged neutral density of H. τ_b is the bounce period. $\vec{\Sigma}$ is a tensor representing ionospheric Hall and Pedersen conductance. Φ and J_{\parallel} are the ionospheric potential and field aligned current. I is the magnetic dip angle.

[11] Equation (7) represents a drift-loss model of the ring current species s with the consideration of charge exchange and loss cone losses. It includes multiple processes of different timescales. We use the method of fractional step or operator splitting to decompose the equation and solve only one term at a fractional step [Fok et al., 1993]. The ionospheric field aligned current in equation (8) is calculated from the nonzero divergence of the perpendicular current contributed by all the ring current species. In this study, both ring current H^+ (originated from solar wind and polar region) and O^+ (originating from auroral region) are considered in the calculation of J_{\parallel} in equation (8). The ionospheric potential along the CRCM polar boundary is calculated by the LFM model. The CRCM polar boundary is set at $\lambda_i = 70.3^\circ$, which is the maximum latitude in the model. Since the CRCM simulation domain is confined in the closed field region, the actual boundary at the ionosphere is limited to the open-closed field boundary. During active period of expanded polar cap, the CRCM polar

boundary can extend to well below 70.3° [Ebihara et al., 2005].

[12] In simulating this particular event on 20–21 November 2003, the CRCM boundary at the magnetic equator is an ellipse with major axis set on the SM x axis. The nightside end of the major axis is placed at $8 R_E$ radial distance and dayside end at the standoff distance, which is the length of the semiminor axis. However, the actual boundary at the equator is the overlapping of the ellipse and the equatorial mapping of the ionospheric boundary. We calculate the total energy content of each ion species inside the CRCM boundary. Figure 5 plots the energy content of 3 ion species during the storm. The corresponding magnetic depression from the ring current estimated by the Dessler-Parker-Sckopke relation [Dessler and Parker, 1959; Sckopke, 1966] is also labeled on the energy axis. symH*, the pressure corrected symH is also shown to compare with the calculated energy and ΔB . In our simulation, solar wind H^+ is always the major supplier to the total ring current energy for this particular storm. The contribution from ionospheric O^+ is significant, especially near the peak of the storm. The role of ionospheric H^+ is very minor in our simulation. In general, the total energy (blue curve) tracks the symH* (red curve) pretty well during the storm. The simulation is able to reproduce the brief recovery around 1200 UT on 20 November and the double-peaks feature at the storm maximum. However, the simulated total energy reaches its peak value 2 h earlier than the time of minimum symH*. The calculated total energy exhibits a two-step recovery: fast recovery in the first 6 h after the peak and then followed by slow recovery. On the other hand, the recovery of symH* does not slow down until 9 h after its minimum value. In section 4, we will examine the possible causes of these discrepancies.

[13] During active times, ions and electrons are transported from the plasma sheet into the ring current region. These newly injected plasmas tend to shield the inner magnetosphere from the external convection field through establishing field aligned currents that connect the ring current region and the subauroral ionosphere [Wolf, 1983; Fok et al., 2003; Ebihara and Fok, 2004]. Figure 6 plots the simulated potential drop at the ionosphere during the storm at the CRCM polar boundary and at 3 magnetic latitudes (mlat) equatorward to the boundary. At given boundary or latitude, the potential drop is estimated by the difference between the maximum potential and the minimum potential across that boundary. In Figure 6, the green curve is the potential drop given by the LFM model at the CRCM polar boundary, which is also the boundary potential in solving equation (8). The blue, red and purple curves are potential drop at 60° , 50° and 40° latitudes, respectively. During the peak of the storm around 1800 UT, the green and blue curves overlap with each other, indicating that the open-closed region is extended to 60° mlat. As shown in Figure 6, the inner magnetosphere is pretty well shielded in the first 12 h of 20 November. The shielding starts to breakdown at 1300 UT. Since then to the end of the day, electric field is strong in the ring current region at mlat $< 60^\circ$. Theoretical studies have shown that magnetic reconfiguration during storm main phase or active periods favors the penetration of high-latitude electric fields [Garner et al., 2004; Wolf et al., 2007]. Our simulation is also consistent with observations

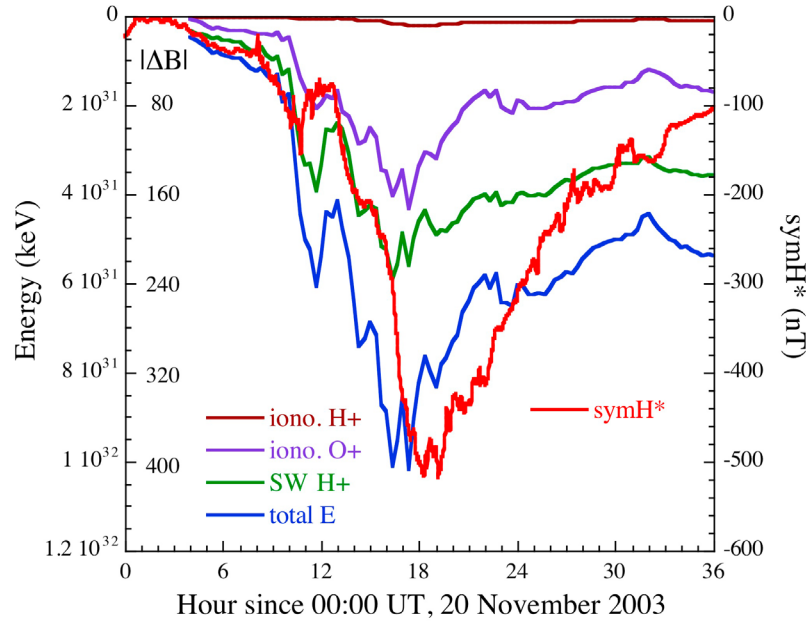


Figure 5. Simulated ring current ion energy content compared with symH^* during the storm on 20–21 November 2003. Notice that the energy axis is pointing down. The corresponding $|\Delta B|$ in nT from the D-P-S relation is also labeled.

reported by *Zhao et al.* [2008] on prompt penetration electric field on 20 November 2003.

[14] Ions and electrons are expected to travel deep earthward in the period of strong penetration electric field. Figure 7 shows the L -time plots of solar wind H^+ and ionospheric O^+ fluxes at the equator during the storm. Noticeable injections of both ion species start at ~ 1000 UT. High fluxes are seen at $L \sim 4$. At ~ 1300 UT, strong penetration field moves ions earthward. At the peak of the storm, ring current ions penetrate as deep as to $L \sim 1.5$. At these low L shells, ions encounter dense geocorona and experience strong charge exchange losses. The decay of O^+ is faster since the charge exchange cross section of O^+ with neutral H is stronger than that of H^+ .

4. Physical Processes Controlling the Storm Development

[15] We have shown in Figure 5 that H^+ outflow from the ionosphere contributes insignificantly to the ring current in this particular storm on 20–21 November 2003. We can treat the solar wind H^+ as the dominant source of H^+ in the hot plasma pressure whose gradient supports the ring current. Likewise, the O^+ outflow represents the dominant source of ring current ions originating from the ionosphere. In our CRCM simulation, we track energy gain and loss of each species due to drift, changing of magnetic field (B) configuration, loss at the loss cone and charge exchange loss. For drift motion, energy content will change when particles are injected into or drift out of the simulation domain. Particle acceleration or deceleration by convection is also accounted as a drift effect. Ions will gain or lose energy by the inductive electric field as magnetic configuration is varying with time. Also, ions will be lost from the system when a closed field line become open and vice versa. In our

model, ions in the loss cone are subject to a fast loss time of half of the bounce period (equation 7). To conserve the second adiabatic invariant, particles originally outside the loss cone may be driven into the loss cone as they drift earthward to shorter field lines. Finally, ions are lost when they experience charge exchange with the geocorona. Only charge exchange of ions with neutral H is considered in this

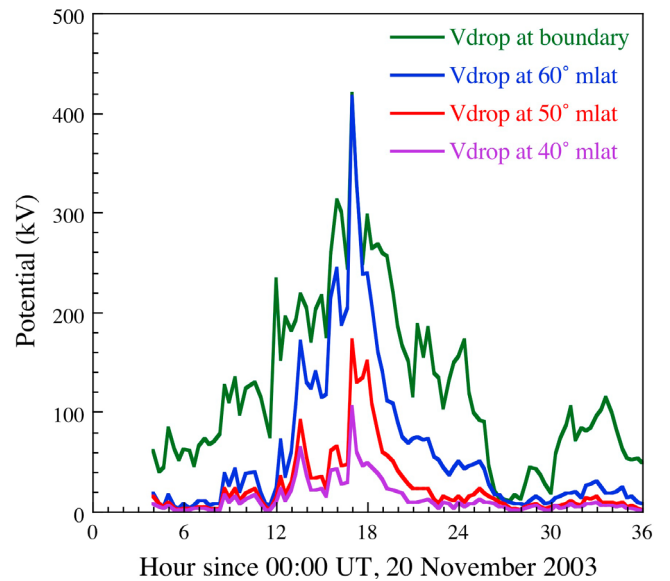


Figure 6. Potential drop at northern ionosphere during the 20–21 November 2003 storm. Green curve is the LFM potential drop across CRCM polar boundary. Blue, red, and purple curves are the CRCM potential drop across 60° , 50° , and 40° mlat, respectively.

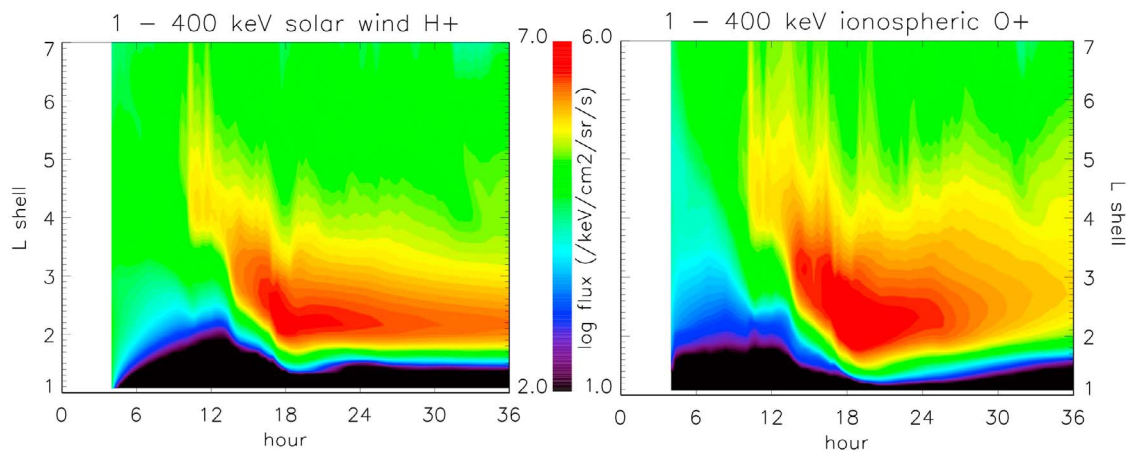


Figure 7. L -time diagrams of (left) solar wind H^+ and (right) ionospheric O^+ fluxes at the equator. Zero hour corresponds to 0000 UT on 20 November 2003.

study, though loss from contact with the much thinner layer of neutral O also occurs, but is localized to the atmospheric loss cone.

[16] We examine the processes that control the growth and decay of ring current H^+ and O^+ during the storm. As mentioned in section 3, equation (7) is decomposed and only one term is solved at a time. Before and after advancing the distribution function of a ring current species at a fractional step, we calculate the total energy content of that ion species. In this way we can estimate the energy gain or loss in one time step due to a particular process. Figure 8 plots the accumulated energy change of H^+ (Figure 8, left) and O^+ (Figure 8, right) from drift, loss cone, charge exchange and time-varying magnetic field. The slope of the total energy curves represents the rate of energy gain

or loss. The total energy content of H^+ (green curve) and O^+ (purple curve) are plotted. The loss cone loss (dark red curves) has only a very minor effect on the total energy budget for either species. The loss cone may play a more important role if pitch angle diffusion due to wave-particle interactions is considered [Jordanova *et al.*, 1998, 2001; Khazanov *et al.*, 2002, 2006]. Charge exchange loss (magenta curves) is the dominant loss mechanism, especially for O^+ . The loss rate is the fastest near the peak of the storm when large amount of ions injected into the ring current region. These freshly injected ions are rich in field-aligned pitch angles [Mauk and McIlwain, 1975; Mauk, 1986; Fok *et al.*, 2006] and thus experience strong charge exchange loss.

[17] The rates of energy change due to time-varying B (black curves in Figure 8) fluctuate considerably throughout

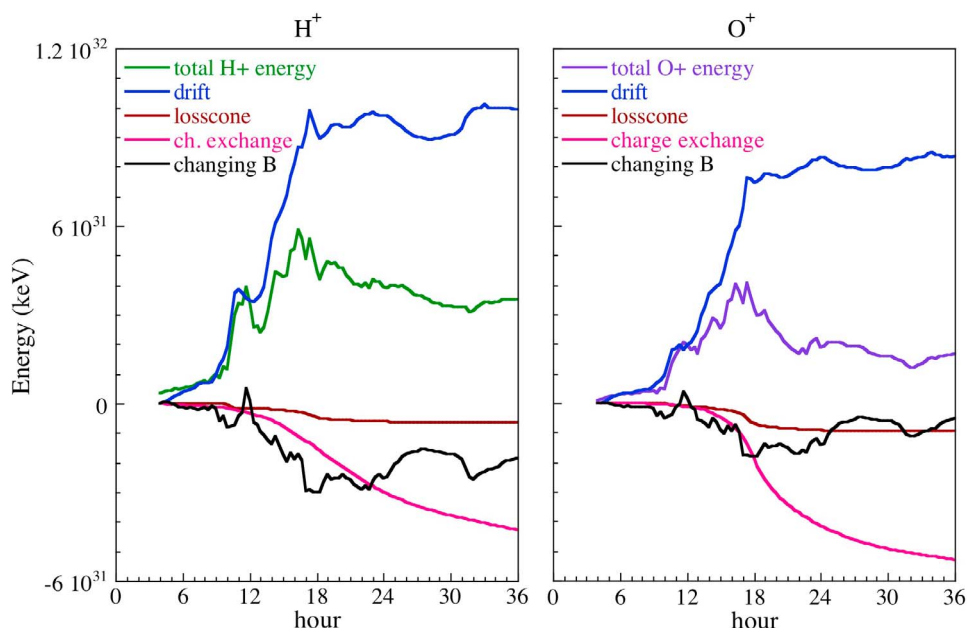


Figure 8. Accumulated energy changes due to various processes during the storm. (left) Ring current H^+ . (right) Ring current O^+ . The total energy contents of H^+ and O^+ also plotted. Zero hour corresponds to 0000 UT on 20 November 2003.

the storm. Highly compressed magnetosphere and strong southward IMF during the main phase produce significant particle loss of magnetopause shadowing [Liemohn *et al.*, 1999; Keika *et al.*, 2005; Ukhorskiy *et al.*, 2006; Ohtani *et al.*, 2009]. Trapped particles will find themselves in the open field region and be lost at the magnetopause. Our results are consistent with the finding by Bortnik *et al.* [2006]. They found a large dropout of relativistic electron flux at $L > 5$ on 20 November 2003. The dropout was energy independent and they explained flux decrease as loss to the magnetopause. Ion drift motion (blue curves) controls the growth of the ring current during the storm main phase. The rapid increase in energy is a combined effect of particle injection and adiabatic acceleration during strong convection. From 6 to 12 h, both the H^+ and O^+ energy contents follow the accumulated energy increase due to drift. In the later half of the main phase (12–18 h), energy growth by drift motion competes with loss from magnetopause shadowing. As a result, total energy contents of H^+ and O^+ reach their peak values at 16 h when energy gains by drift are still growing. This difference in timing explains the time shift between the peaks of our calculated ring current energy content and the observed symH* (Figure 5). Overall, drift motion dominates the variations of ring current energy content during the main phase and charge exchange loss dominates in the recovery phase. Our model predicts a slower recovery than that from the observed symH* (Figure 5). We anticipate the model-data comparison will be improved when wave associated loss is included in the model. This will be a subject of future work.

5. Discussion

[18] We report here a global simulation study of an unusually large geospace storm (superstorm) with a peak ring current magnitude (storm time depression or Dst) of more than 400 nT. We use a simulation scheme including a global MHD simulation of the solar wind interaction with the magnetosphere and ionosphere via field-aligned currents. This interaction is used to drive ionospheric outflows according to an empirical scheme that used electromagnetic and kinetic fluxes into the ionosphere, imposed by the global simulation, to drive local ionospheric outflow fluxes of oxygen ion plasma. Polar wind outflows of protons are also included. The ionospheric plasmas are circulated through the MHD field using a single particle trajectory code using a Monte Carlo method to initiate representative particles, track them through the simulation, and compute their bulk or kinetic properties at any region where this information is needed.

[19] Embedded within the outer magnetosphere simulation is a ring current simulation based on the CRCM, a bounce-averaged kinetic Boltzmann equation treatment, with results as shown in Figure 5. Here we see that the simulation matches well the observed total energy in the storm ring current. The inner magnetospheric simulation is driven electromagnetically at its outer boundary by the MHD outer magnetospheric simulation, which produces the imposed transpolar potential drop. Very large potentials were developed for this storm, as shown in Figure 6. The inner magnetosphere was supplied by plasma at its boundary by the combination of the MHD solar wind and the ionospheric

outflows of protons and oxygen. The simulation then follows the flow of these plasmas through the inner magnetosphere, accounting for their energization and loss processes. We find that even in this very large storm, the oxygen contribution to the ring current is comparable to, but slightly less than, the hydrogen (solar wind, mainly) contribution, as measured by the total energy stored, or by symH* (proxy for Dst).

[20] This result is somewhat surprising and diverges from recent observations, for example those reported by Nosé *et al.* [2005] or Mitchell *et al.* [2003]. From those results, and from the substantial contributions of oxygen in our earlier work on substorms and smaller storms [Fok *et al.*, 2006; Moore *et al.*, 2008], we anticipated that we might find that oxygen would essentially take over the ring current for such a large event, but that is not the case here. These results, appearing in various forms in Figures 5, 7, and 8, show that oxygen exceeded 50% of the proton energy for much of the storm period, reaching about 90% of the proton energy content at the peak of the storm.

[21] There are several possible interpretations of the simulated oxygen content deficiency relative to observations of large storms. First is the possibility that our oxygen outflow model saturates or otherwise fails to produce as much oxygen outflow as actually occurs during such large events. Second, it is possible that the transport paths of the oxygen outflows in our simulation do not supply enough oxygen to the places where it is energized into the ring current population. Third, it is possible that our simulation does not sufficiently energize the oxygen present within the simulation to cause it to dominate the proton contribution.

[22] To illustrate these considerations, we introduce Figure 9 comparing the simulated (Figure 9, left) and observed by Geotail (Figure 9, right) species energy densities and Bz GSM along the path of Geotail for this specific storm. Geotail was moving very close to the CRCM tailward boundary from 1600 to 2200 UT. The Geotail ion data are taken from the SupraThermal Ion Composition Spectrometer (STICS) sensor of the Energetic Particle and Ion Composition (EPIC) instrument [Williams *et al.*, 1994]. STICS provides mass and charge state information of ions and covers the E/Q range of 9 to 210 keV/e. Energy density is calculated using the same method as Nosé *et al.* [2003]. The Geotail orbit segment is shown in Figure 9 (bottom right), while the simulated storm main phase ratio of O^+/H^+ ring current energy is shown in Figure 9 (bottom left). The period of the Geotail observations is shown by the red box with arrows indicating the temporal relationship of the Geotail observations to the full storm evolution of species energy content. As shown in Figure 9 (top), the GIK simulated H^+ and O^+ energy density are similar in magnitude, and are comparable with the H^+ energy density measured by Geotail. However, the observed O^+ energy density is significantly higher than that from the simulation.

[23] From our previous experience with applying the Strangeway *et al.* [2005] outflow scaling globally, we consider it unlikely that insufficient oxygen outflows are occurring in our simulation. The scaling does not saturate for high values of either Poynting flux or electron precipitation, and the area over which high values are found increases substantially with the overall magnitude of the event. Moreover, the transport pathways for ionospheric outflows in

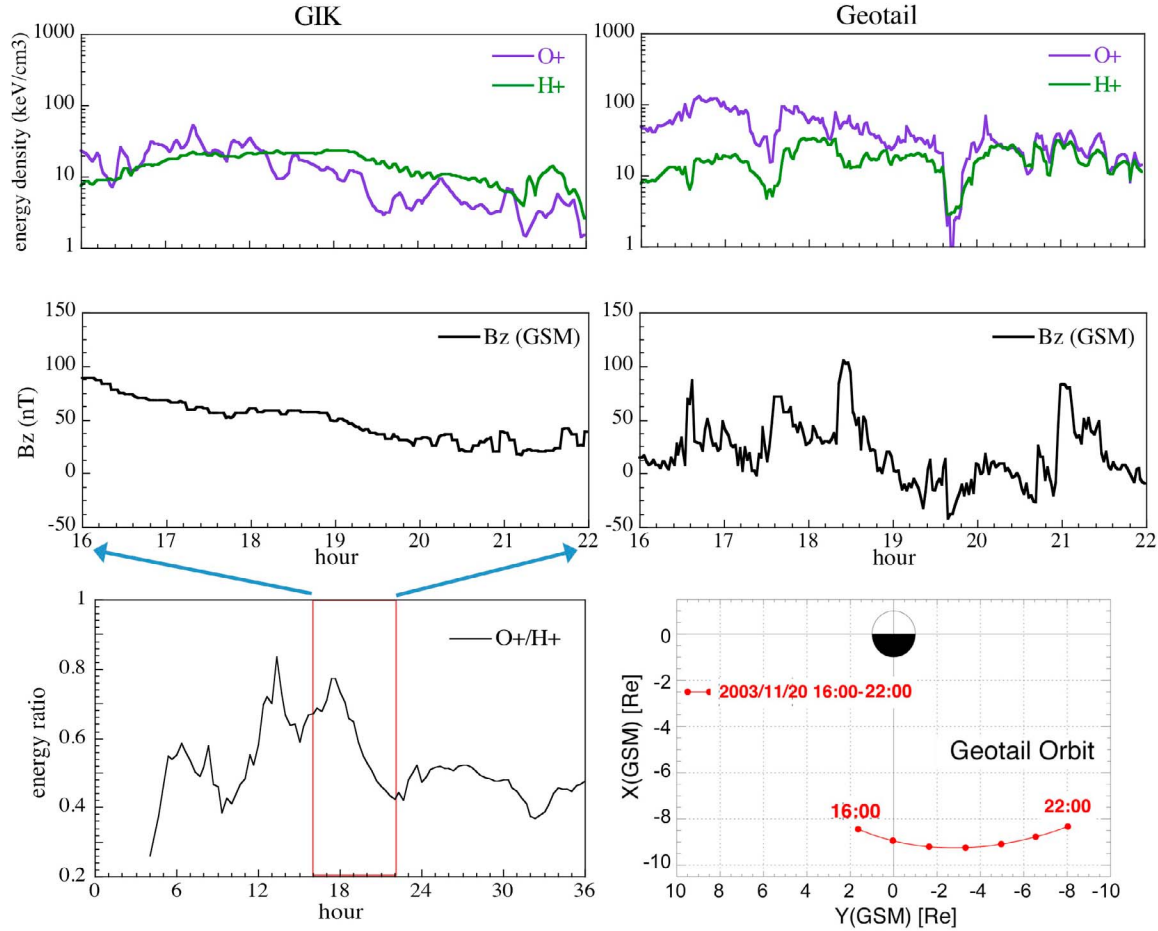


Figure 9. Comparison of simulated and observed parameters: (top) energy density, (middle) GSM Bz, (bottom left) simulated ring current energy ratio, and (bottom right) Geotail orbit segment during the storm on 20 November 2003.

these simulations are known to feed directly to the central plasma sheet and thenceforth into the inner magnetosphere via the midnight sector, for southward IMF. Thus we consider the most likely explanation for this discrepancy to be a lack of sufficient acceleration of oxygen by the MHD fields. As reported by *Mitchell et al.* [2003], it is known that substorm dipolarizations accelerate oxygen more effectively than protons into the ring current region. Such an effect could well produce enhanced oxygen energy content, with lower proton energy content, in the main phase ring current. The MHD fields we use here include a measure of dipolarization in association with magnetotail dynamics during this storm. However, the simulated field behavior is far more gentle and less abrupt than is observed, as may readily be confirmed in Figure 9, and it clearly has a comparable effect on the protons and oxygen ions.

[24] Thus it is possible that the highest contributions of oxygen ring current content are produced by substorm dipolarization effects acting in combination with an enhanced source of oxygen plasma from the auroral ionosphere. Thus, the decreasing trend in the O^+ energy density in the second half of the storm can be largely attributed to a reduction of energization processes in the simulation. By contrast, the observations show a magnetic field at the spacecraft location

that is generally much more variable than in the simulation, with large amplitude nearly discontinuous jumps in strength. Thus, our MHD simulation is failing to fully capturing the substorm like changes in the magnetotail [Aggson *et al.*, 1983], and these are known to strongly affect ion energization in this region [Nosé *et al.*, 2000, 2009a]. Imposed dipolarization can and have been applied to mimic substorm reconfiguration and the corresponding particle acceleration. *Delcourt* [2002] simulated the substorm expansion phase using a smooth few-minute transition of an empirical magnetic field model from a disturbed or highly stretched level to a relatively undisturbed or less stretched one. Oxygen ions were found to experience nonadiabatic energization in the dipolarizing plasma sheet. Other substorm modeling approaches include, for example, adding current loops to a prescribed magnetic field model to represent substorm current wedge [Yang *et al.*, 2008], or injecting low-content plasma bubble from the plasma sheet into the inner magnetosphere [Zhang *et al.*, 2009].

[25] To examine the effects of substorm energization of O^+ in ring current development, an additional CRCM run has been performed with the O^+ energy density scaled based on Geotail observations. As shown in Figure 9, Geotail was close to the CRCM outer boundary from 16 to 22 h. In this

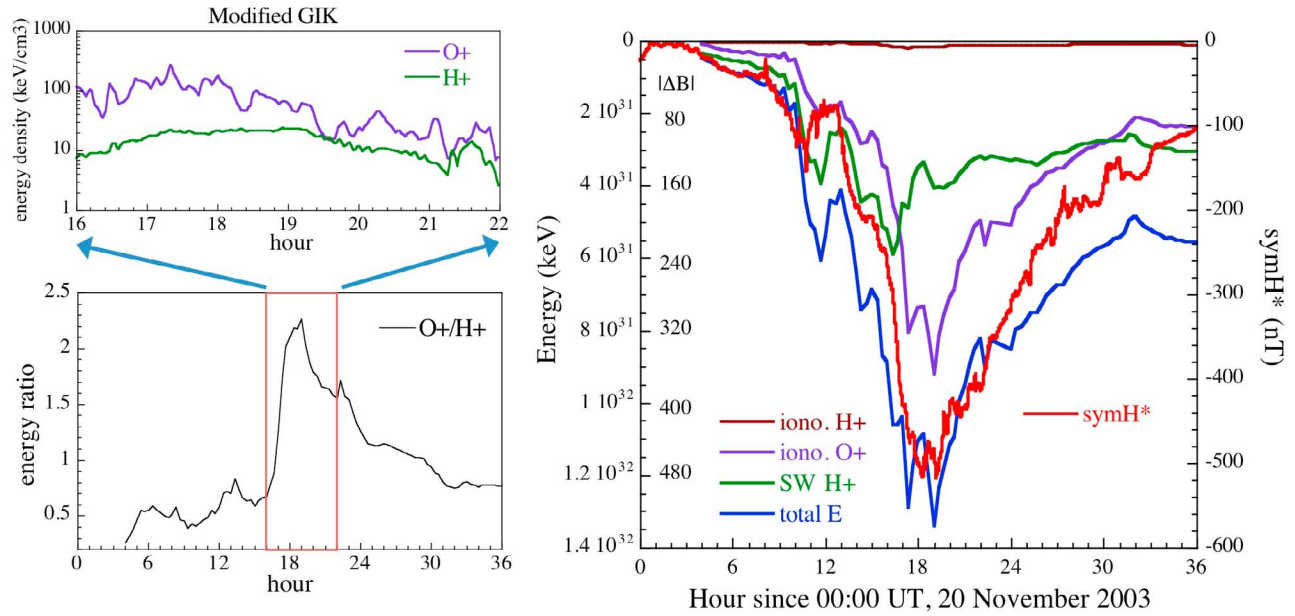


Figure 10. CRCM results with O⁺ energy density at outer boundary at the equator multiplied by 5 from 16 to 22 h. (top left) The corresponding O⁺ and H⁺ density along the Geotail orbit. (bottom left) The calculated energy ratio of ring current O⁺ and H⁺. (right) The same format as Figure 5 except for this new CRCM run.

time period, we increase the O⁺ energy density a factor of 5 at the CRCM boundary at all local times. The scaling factor is ramping up linearly from 1 to 5 in 1500–1600 UT and decreases from 5 to 1 in one hour after 2200 UT. Figure 10 (top left) shows the corresponding O⁺ and H⁺ energy density along the Geotail orbit. The modified O⁺ energy densities are very much comparable to those measured by Geotail. The same H⁺ energy densities from the LFM model are used in the new CRCM run. Figure 10 (right) plots the energy contents of each ring current ion species calculated by the CRCM. With enhanced distribution at the model boundary, O⁺ energy content increases rapidly beginning at 16 h and exceeds the energy of H⁺ at 17 h. The O⁺ energy continues to increase and displays a double-dips feature, consistent with the observed symH*. After reaching the peak, O⁺ ions experience a fast decay owing to charge exchange loss and the total energy content becomes comparable with that of H⁺ at 30 h. The total energy (blue curve) calculated from this CRCM run follows very well with the symH* index (red curve). The fast decay in the first 10 h of recovery is closely reproduced, with much better agreement than the result shown in Figure 5. The estimated magnetic depression from the ring current also fully accounts for the observed symH*. Figure 10 (bottom left) plots the calculated energy ratio of O⁺ to H⁺. The ratio reaches a high value of 2.3 at the peak of the storm at 19 h, consistent with ion observations in the ring current region during major storms [Hamilton *et al.*, 1988; Nosé *et al.*, 2009b]. This new CRCM run clearly demonstrates the importance of accurate representation of substorm energization, especially for heavy ions, in modeling the ring current.

[26] This study involves a collection of simulation tools: global MHD model, kinetic model of the ring current and test-particle calculation. The couplings between these models are

basically one directional and no mutual interactions from one to another. For example, the pressure generated from the hot ring current ions is not fed back to the LFM model. The O⁺ outflow from the ionosphere may affect the global magnetospheric configuration and dynamics, but these effects are not considered in this paper. Recent efforts have been made to couple the important regions in the magnetosphere in a more consistent and bidirectional manner [De Zeeuw *et al.*, 2004; Gloer *et al.*, 2009; Zaharia *et al.*, 2006]. This is also a goal for our future studies.

6. Conclusions

[27] Comparing our GIK simulation of the ring current for an unusually large geospace storm with observations of this and other such storms, we conclude the following:

[28] 1. The simulation produces a ring current whose magnitude is in good agreement with the observed ring current as measured by symH*, a proxy for Dst.

[29] 2. Without oxygen from ionospheric outflows, the ring current would have been too small by about 50% of the observed ring current magnitude.

[30] 3. Despite expectations from observations of other events, the oxygen content contributed significantly, but did not overwhelm the solar wind protons in the simulated storm. Direct comparisons with observations of this storm by the Geotail spacecraft indicate that the MHD simulation did not fully capture the large amplitude magnetic fluctuations associated with individual substorms, suggesting that simulated O⁺ energy densities are lower than they would be if this magnetotail behavior could be fully described.

[31] 4. CRCM simulation with O⁺ energy density at the boundary set comparable to Geotail observations produces excellent agreement with the observed symH*. As expected

in superstorms, ring current O^+ is the dominant species over H^+ during the main to midrecovery phase of the storm.

[32] It seems clear from these results that future updates of global simulation codes should seek to more realistically produce the large amplitude substorm reconfigurations of the magnetotail that are associated with highly disturbed storm periods. Such improvements should help to improve the agreement between our simulations and observations of such storms.

[33] **Acknowledgments.** We gratefully acknowledge use of the ACE solar wind data provided through OMNI and Geotail data from <http://sd-www.jhuapl.edu/Geotail/>. The Dst and symH data are provided by the World Data Center for Geomagnetism, Kyoto, Japan. We would like to thank Natalia Buzulukova for valuable comments. We also thank Manuel Buenfil and Robert Wiegand for performing the test-particle and bulk parameter calculations. We acknowledge support from the NASA Heliophysics Division through the ROSES program under Work Breakdown Structures 936723.02.01.03.82 and 955518.02.01.02.57, and NASA's High Performance Computing Program under task R0608.

[34] Masaki Fujimoto thanks the reviewers for their assistance in evaluating this paper.

References

- Aggson, T. L., J. P. Heppner, and N. C. Maynard (1983), Observations of large magnetospheric electric fields during the onset phase of a substorm, *J. Geophys. Res.*, **88**, 3981–3990, doi:10.1029/JA088iA05p03981.
- Barakat, A. R., R. W. Schunk, T. E. Moore, and J. H. Waite Jr. (1987), Ion escape fluxes from the terrestrial high-latitude ionosphere, *J. Geophys. Res.*, **92**, 12,255–12,266, doi:10.1029/JA092iA11p12255.
- Bortnik, J., R. M. Thorne, T. P. O'Brien, J. C. Green, R. J. Strangeway, Y. Y. Shprits, and D. N. Baker (2006), Observation of two distinct, rapid loss mechanisms during the 20 November 2003 radiation belt dropout event, *J. Geophys. Res.*, **111**, A12216, doi:10.1029/2006JA011802.
- Chen, M. W., and M. Schulz (2001), Simulations of diffuse aurora with plasma sheet electrons in pitch angle diffusion less than everywhere strong, *J. Geophys. Res.*, **106**, 28,949–28,966, doi:10.1029/2001JA000138.
- Delcourt, D. C. (2002), Particle acceleration by inductive electric fields in the inner magnetosphere, *J. Atmos. Sol. Terr. Phys.*, **64**, 551–559, doi:10.1016/S1364-6826(02)00012-3.
- Delcourt, D. C., J. A. Sauvaud, and A. Pedersen (1990), Dynamics of single particle orbits during substorm expansion phase, *J. Geophys. Res.*, **95**, 20,853–20,865, doi:10.1029/JA095iA12p20853.
- Dessler, A. J., and E. N. Parker (1959), Hydromagnetic theory of geomagnetic storms, *J. Geophys. Res.*, **64**, 2239–2252, doi:10.1029/JZ064i012p02239.
- De Zeeuw, D. L., S. Sazykin, R. A. Wolf, T. I. Gombosi, A. J. Ridley, and G. Toth (2004), Coupling of a global MHD code and an inner magnetospheric model: Initial results, *J. Geophys. Res.*, **109**, A12219, doi:10.1029/2003JA010366.
- Ebihara, Y., and M.-C. Fok (2004), Post-midnight storm-time enhancement of tens-of-keV proton flux, *J. Geophys. Res.*, **109**, A12209, doi:10.1029/2004JA010523.
- Ebihara, Y., M.-C. Fok, S. Sazykin, M. F. Thomsen, M. R. Hairston, D. S. Evans, F. J. Rich, and M. Ejiri (2005), Ring current and the magnetosphere-ionosphere coupling during the superstorm of 20 November 2003, *J. Geophys. Res.*, **110**, A09S22, doi:10.1029/2004JA010924.
- Fedder, J. A., J. G. Lyon, S. P. Slinker, and C. M. Mobarry (1995), Topological structure of the magnetotail as a function of interplanetary magnetic field direction, *J. Geophys. Res.*, **100**, 3613–3621, doi:10.1029/94JA02577.
- Fok, M.-C., J. U. Kozyra, A. F. Nagy, C. E. Rasmussen, and G. V. Khazanov (1993), Decay of equatorial ring current ions and associated aeronomical consequences, *J. Geophys. Res.*, **98**, 19,381–19,393, doi:10.1029/93JA01848.
- Fok, M.-C., R. A. Wolf, R. W. Spiro, and T. E. Moore (2001), Comprehensive computational model of the Earth's ring current, *J. Geophys. Res.*, **106**, 8417–8424, doi:10.1029/2000JA000235.
- Fok, M.-C., et al. (2003), Global ENA IMAGE simulations, *Space Sci. Rev.*, **109**, 77–103, doi:10.1023/B:SPAC.0000007514.56380.fid.
- Fok, M.-C., T. E. Moore, P. C. Brandt, D. C. Delcourt, S. P. Slinker, and J. A. Fedder (2006), Impulsive enhancements of oxygen ions during substorms, *J. Geophys. Res.*, **111**, A10222, doi:10.1029/2006JA011839.
- Foster, J. C., et al. (2005), Multiradar observations of the polar tongue of ionization, *J. Geophys. Res.*, **110**, A09S31, doi:10.1029/2004JA010928.
- Garner, T. W., R. A. Wolf, R. W. Spiro, W. J. Burke, B. G. Fejer, S. Sazykin, J. L. Roeder, and M. R. Hairston (2004), Magnetospheric electric fields and plasma sheet injection to low L-shells during the 4–5 June 1991 magnetic storm: Comparison between the Rice Convection Model and observations, *J. Geophys. Res.*, **109**, A02214, doi:10.1029/2003JA010208.
- Glocer, A., G. Toth, Y. Ma, T. Gombosi, J. Zhang, and L. M. Kistler (2009), Multifluid Block-Adaptive-Tree Solar wind Roe-type Upwind Scheme: Magnetospheric composition and dynamics during geomagnetic storms—Initial results, *J. Geophys. Res.*, **114**, A12203, doi:10.1029/2009JA014418.
- Hamilton, D. C., G. Gloeckler, F. M. Ipavich, W. Studemann, B. Wilken, and G. Kremser (1988), Ring current development during the great geomagnetic storm of February 1986, *J. Geophys. Res.*, **93**, 14,343–14,355, doi:10.1029/JA093iA12p14343.
- Hecht, J. H., et al. (2008), Satellite and ground-based observations of auroral energy deposition and the effects on thermospheric composition during large geomagnetic storms: 1. Great geomagnetic storm of 20 November 2003, *J. Geophys. Res.*, **113**, A01310, doi:10.1029/2007JA012365.
- Jordanova, V. K., C. J. Farrugia, J. M. Quinn, R. M. Thorne, K. W. Ogilvie, R. P. Lepping, G. Lu, A. J. Lazarus, M. F. Thomsen, and R. D. Belian (1998), Effect of wave-particle interactions on ring current evolution for January 10–11, 1997: Initial results, *Geophys. Res. Lett.*, **25**, 2971–2974, doi:10.1029/98GL00649.
- Jordanova, V. K., C. J. Farrugia, R. M. Thorne, G. V. Khazanov, G. D. Reeves, and M. F. Thomsen (2001), Modeling ring current proton precipitation by electromagnetic ion cyclotron waves during the May 14–16, 1997, storm, *J. Geophys. Res.*, **106**, 7–22, doi:10.1029/2000JA002008.
- Keika, K., M. Nosé, S.-I. Ohtani, K. Takahashi, S. P. Christon, and R. W. McEntire (2005), Outflow of energetic ions from the magnetosphere and its contribution to the decay of the storm time ring current, *J. Geophys. Res.*, **110**, A09210, doi:10.1029/2004JA010970.
- Khazanov, G. V., K. V. Gamayunov, V. K. Jordanova, and E. N. Krivovutsky (2002), A self-consistent model of the interacting ring current ions and electromagnetic ion cyclotron waves, initial results: Waves and precipitation fluxes, *J. Geophys. Res.*, **107**(A6), 1085, doi:10.1029/2001JA000180.
- Khazanov, G. V., K. V. Gamayunov, D. L. Gallagher, and J. U. Kozyra (2006), Self-consistent model of magnetospheric ring current and propagating electromagnetic ion cyclotron waves: Waves in multi-ion magnetosphere, *J. Geophys. Res.*, **111**, A10202, doi:10.1029/2006JA011833.
- Liemohn, M. W., J. U. Kozyra, V. K. Jordanova, G. V. Khazanov, M. F. Thomsen, and T. E. Cayton (1999), Analysis of early phase ring current recovery mechanisms during geomagnetic storms, *Geophys. Res. Lett.*, **26**, 2845–2848, doi:10.1029/1999GL000611.
- Lyons, L. R. (1981), The field-aligned current versus electric potential relation and auroral electrodynamics, in *Physics of Auroral Arc Formation*, *Geophys. Monogr. Ser.*, vol. 25, edited by S.-I. Akasofu and J. R. Kan, pp. 252–259, AGU, Washington, D. C.
- Mauk, B. H. (1986), Quantitative modeling of the “convection surge” mechanism of ion acceleration, *J. Geophys. Res.*, **91**, 13,423–13,431, doi:10.1029/JA091iA12p13423.
- Mauk, B. H., and C. E. McIlwain (1975), UCSD auroral particles experiment, *IEEE Trans. Aerosp. Electron. Syst.*, **AES-11**, 1125–1130, doi:10.1109/TAES.1975.308164.
- Mitchell, D. G., P. C. Brandt, E. C. Roelof, D. C. Hamilton, K. Retterer, and S. Mende (2003), Global Imaging of O^+ from IMAGE/HENA, *Space Sci. Rev.*, **109**, 63–75, doi:10.1023/B:SPAC.0000007513.55076.00.
- Mobarry, C. M., J. A. Fedder, and J. G. Lyon (1996), Equatorial plasma convection from global simulations of the Earth's magnetosphere, *J. Geophys. Res.*, **101**, 7859–7874, doi:10.1029/95JA02301.
- Moore, T. E., M.-C. Fok, D. C. Delcourt, S. P. Slinker, and J. A. Fedder (2007), Global aspects of solar wind-ionosphere interactions, *J. Atmos. Sol. Terr. Phys.*, **69**(3), 265–278, doi:10.1016/j.jastp.2006.08.009.
- Moore, T. E., M.-C. Fok, D. C. Delcourt, S. P. Slinker, and J. A. Fedder (2008), Plasma plume circulation and impact in an MHD substorm, *J. Geophys. Res.*, **113**, A06219, doi:10.1029/2008JA013050.
- Nosé, M., A. T. Y. Lui, S. Ohtani, B. H. Mauk, R. W. McEntire, D. J. Williams, T. Mukai, and K. Yumoto (2000), Acceleration of oxygen ions of ionospheric origin in the near-Earth magnetotail during substorms, *J. Geophys. Res.*, **105**, 7669–7677, doi:10.1029/1999JA000318.
- Nosé, M., R. W. McEntire, and S. P. Christon (2003), Change of the plasma sheet ion composition during magnetic storm development observed by the Geotail spacecraft, *J. Geophys. Res.*, **108**(A5), 1201, doi:10.1029/2002JA009660.
- Nosé, M., S. Taguchi, K. Hosokawa, S. P. Christon, R. W. McEntire, T. E. Moore, and M. R. Collier (2005), Overwhelming O^+ contribution to the plasma sheet energy density during the October 2003 superstorm: Geotail/

- EPIC and IMAGE/LENA observations, *J. Geophys. Res.*, **110**, A09S24, doi:10.1029/2004JA010930.
- Nosé, M., S. Taguchi, S. P. Christon, M. R. Collier, T. E. Moore, C. W. Carlson, and J. P. McFadden (2009a), Response of ions of ionospheric origin to storm time substorms: Coordinated observations over the ionosphere and in the plasma sheet, *J. Geophys. Res.*, **114**, A05207, doi:10.1029/2009JA014048.
- Nosé, M., A. Ieda, and S. P. Christon (2009b), Geotail observations of plasma sheet ion composition over 16 years: On variations of average plasma ion mass and O⁺ triggering substorm model, *J. Geophys. Res.*, **114**, A07223, doi:10.1029/2009JA014203.
- Ohtani, S., Y. Miyoshi, H. J. Singer, and J. M. Weygand (2009), On the loss of relativistic electrons at geosynchronous altitude: Its dependence on magnetic configurations and external conditions, *J. Geophys. Res.*, **114**, A01202, doi:10.1029/2008JA013391.
- Scokopke, N. (1966), A general relation between the energy of trapped particles and the disturbance field near the Earth, *J. Geophys. Res.*, **71**, 3125–3130.
- Slinker, S. P., J. A. Fedder, J. Chen, and J. G. Lyon (1998), Global MHD simulation of the magnetosphere and ionosphere for 1930–2330 UT on November 3, 1993, *J. Geophys. Res.*, **103**, 26,243–26,250, doi:10.1029/97JA02775.
- Slinker, S. P., J. A. Fedder, J. M. Ruohoniemi, and J. G. Lyon (2001), Global MHD simulation of the magnetosphere for November 24, 1996, *J. Geophys. Res.*, **106**, 361–380, doi:10.1029/2000JA000603.
- Strangeway, R. J., C. T. Russell, C. W. Carlson, J. P. McFadden, R. E. Ergun, M. Temerin, D. M. Klumpp, W. K. Peterson, and T. E. Moore (2000), Cusp field-aligned currents and ion outflows, *J. Geophys. Res.*, **105**(A9), 21,129–21,141, doi:10.1029/2000JA900032.
- Strangeway, R. J., R. E. Ergun, Y.-J. Su, C. W. Carlson, and R. C. Elphic (2005), Factors controlling ionospheric outflows as observed at intermediate altitudes, *J. Geophys. Res.*, **110**, A03221, doi:10.1029/2004JA010829.
- Su, Y.-J., J. L. Horwitz, T. E. Moore, B. L. Giles, M. O. Chandler, P. D. Craven, M. Hirahara, and C. J. Pollock (1998), Polar wind survey with Thermal Ion Dynamics Experiment/Plasma Source Instrument suite aboard POLAR, *J. Geophys. Res.*, **103**, 29,305–29,337, doi:10.1029/98JA02662.
- Tsyganenko, N. A., and D. P. Stern (1996), Modeling the global magnetic field of the large-scale Birkeland current systems, *J. Geophys. Res.*, **101**, 27,187–27,198, doi:10.1029/96JA02735.
- Ukhorskiy, A. Y., B. J. Anderson, P. C. Brandt, and N. A. Tsyganenko (2006), Storm time evolution of the outer radiation belt: Transport and losses, *J. Geophys. Res.*, **111**, A11S03, doi:10.1029/2006JA011690.
- Williams, D. J., R. W. McEntire, C. Schlemm II, A. T. Y. Lui, G. Gloeckler, S. P. Christon, and F. Gliem (1994), Geotail energetic particles and ion composition instrument, *J. Geomagn. Geoelectr.*, **46**, 39–57.
- Wolf, R. A. (1983), The quasi-static (slow-flow) region of the magnetosphere, in *Solar Terrestrial Physics*, edited by R. L. Carovillano and J. M. Forbes, pp. 303–368, D. Reidel, Norwell, Mass.
- Wolf, R. A., R. W. Spiro, S. Sazykin, and F. R. Toffoletto (2007), How the Earth's inner magnetosphere works: An evolving picture, *J. Atmos. Sol. Terr. Phys.*, **69**, 288–302, doi:10.1016/j.jastp.2006.07.026.
- Yang, J., F. R. Toffoletto, R. A. Wolf, S. Sazykin, R. W. Spiro, P. C. Brandt, M. G. Henderson, and H. U. Frey (2008), Rice Convection Model simulation of the 18 April 2002 sawtooth event and evidence for interchange instability, *J. Geophys. Res.*, **113**, A11214, doi:10.1029/2008JA013635.
- Zaharia, S. V., V. K. Jordanova, M. F. Thomsen, and G. D. Reeves (2006), Self-consistent modeling of magnetic fields and plasma in the inner magnetosphere: Application to a geomagnetic storm, *J. Geophys. Res.*, **111**, A11S14, doi:10.1029/2006JA011619.
- Zhang, J.-C., R. A. Wolf, R. W. Spiro, G. M. Erickson, S. Sazykin, F. R. Toffoletto, and J. Yang (2009), Rice Convection Model simulation of the substorm-associated injection of an observed plasma bubble into the inner magnetosphere: 2. Simulation results, *J. Geophys. Res.*, **114**, A08219, doi:10.1029/2009JA014131.
- Zhao, B., et al. (2008), Ionosphere disturbances observed throughout Southeast Asia of the superstorm of 20–22 November 2003, *J. Geophys. Res.*, **113**, A00A04, doi:10.1029/2008JA013054.
- Zheng, Y., T. E. Moore, F. S. Mozer, C. T. Russell, and R. J. Strangeway (2005), Polar study of ionospheric ion outflow versus energy input, *J. Geophys. Res.*, **110**, A07210, doi:10.1029/2004JA010995.

S.-H. Chen, M.-C. Fok, and T. E. Moore, NASA Goddard Space Flight Center, Code 673, Bldg. 21, Rm. 248, Greenbelt, MD 20771, USA. (meiching.h.fok@nasa.gov)

D. C. Delcourt, Laboratoire de Physique des Plasmas, UMR 7648, Ecole Polytechnique, CNRS, 4 Ave. de Neptune, F-91107 Saint-Maur-des-Fossés, France.

J. A. Fedder, Leading Edge Technology, Inc., 1806 Rampart Dr., Alexandria, VA 22308, USA.

M. Nosé, Data Analysis Center for Geomagnetism and Space Magnetism, Graduate School of Science, Kyoto University, Kitashirakawa-Oiwakecho, Sakyo-ku, Kyoto 606-8502, Japan.

S. P. Slinker, Naval Research Laboratory, Washington, DC 20375, USA.